NeuroImage: Clinical 25 (2020) 102150

Contents lists available at ScienceDirect

NeuroImage: Clinical

journal homepage: www.elsevier.com/locate/ynicl

Novel data-driven, equation-free method captures spatio-temporal patterns of neurodegeneration in Parkinson's disease: Application of dynamic mode decomposition to PET

Jessie Fanglu Fu[a,*], Ivan S. Klyuzhin[b], Martin J. McKeown[b,c], A. Jon Stoessl[b,c], Vesna Sossi[a]

[a] Department of Physics and Astronomy, University of British Columbia, Vancouver, BC, Canada
[b] Division of Neurology, Department of Medicine, University of British Columbia, Vancouver, BC, Canada
[c] Djavad Mowafaghian Centre for Brain Health, Pacific Parkinson's Research Centre, University of British Columbia & Vancouver Coastal Health, Vancouver, BC, Canada

ARTICLE INFO

Keywords:
Novel pattern analysis
Spatio-temporal patterns
Parkinson's disease
Dopaminergic system

ABSTRACT

Most neurodegenerative disorders are characterized by progressive loss of neurons throughout the course of disease in the form of specific spatio-temporal patterns. To capture and quantify these coherent patterns across both space and time, traditionally one would either fit a pre-defined model with spatial and temporal parameters or apply analysis in the spatial and temporal domains separately. In this work, we introduce and validate the use of dynamic mode decomposition (DMD), a data-driven multivariate approach, to extract coupled spatio-temporal patterns simultaneously.

We apply the method to examine progressive dopaminergic degeneration in 41 patients with Parkinson's disease (PD) using [^{11}C](±)dihydrotetrabenazine (DTBZ) Positron Emission Tomography (PET). DMD decomposed the progressive dopaminergic changes in the putamen into two orthogonal temporal progression curves associated with distinct spatial patterns: 1) an anterior-posterior gradient, the expression of which decreased gradually with disease progression with a higher initial expression in the less affected side; 2) a dorsal-ventral gradient in the less affected side, which was present in early disease stage only. In the caudate, we found a head-tail gradient analogous to the anterior-posterior gradient seen in the putamen; as in the putamen, the expression of this gradient decreased gradually with disease progression with higher expression in the less affected side.

Our results with DTBZ PET data show the applicability and relevance of the proposed method for extracting spatio-temporal patterns of neurotransmitter changes due to neurodegeneration. The method is able to decompose known PD-induced dopaminergic denervation into orthogonal (and thus loosely independent) temporal curves, which may be able to reflect and separate either different mechanisms underlying disease progression and disease initiation, or differential involvement of striatal sub-regions at different disease stages, in a completely data driven way. It is expected that this method can be easily extended to other PET tracers and neurodegenerative disorders and may help to elucidate disease mechanisms in more details compared to traditional approaches.

1. Introduction

Many neurodegenerative diseases are characterized by progressive loss of neurons and/or nerve terminals throughout the course of disease in the form of specific spatio-temporal patterns, in which neurodegeneration in different brain regions or network of brain regions may follow distinctive temporal disease progression. Non-invasive neuroimaging techniques such as Positron Emission Tomography (PET) and Single-Photon Emission Computed Tomography (SPECT) are often used to track disease progression and to better understand disease mechanisms. Many attempts have been made to explore spatio-temporal patterns of disease progression using PET or SPECT. One common approach is to fit an exponential or another appropriate model with a fixed number of spatial and temporal parameters to tracer binding values. Previous studies have explored the spatio-temporal patterns of dopaminergic denervation at both individual regions of interest (ROI) level (Colloby et al., 2005; Nandhagopal et al., 2009) and at the voxel level (Badoud et al., 2016; Klyuzhin et al., 2019) using several

* Corresponding author.
E-mail address: jfu@phas.ubc.ca (J.F. Fu).

https://doi.org/10.1016/j.nicl.2019.102150
Received 11 October 2019; Received in revised form 16 December 2019; Accepted 26 December 2019
Available online 27 December 2019

dopaminergic PET tracers and ^{123}I-ioflupane SPECT. However, with this approach, the progressive spatial patterns are either limited to a set of pre-defined ROIs, or to being along a specific spatial axis within a brain structure. Data-driven multivariate approaches have also been recently used to extract and visualize spatial patterns of tracer binding values, mainly using dimension reduction techniques such as principal component analysis (PCA) (Klyuzhin et al., 2018) or independent component analysis (ICA). One major constraint associated with these methods is that PCA and ICA are temporally static techniques and do not model the temporal progression of the spatial patterns. One needs to assume that the spatial patterns obtained with PCA or ICA remain static/constant over time and only the expression of these spatial patterns increases or decreases as disease progresses; this assumption may not necessarily be valid or in keeping with the fundamental nature of the disease.

We introduce and validate the use of dynamic mode decomposition (DMD) to extract spatial patterns of tracer binding values associated with distinctive and orthogonal temporal disease progression curves. DMD is a relatively new decomposition method first developed in the field of fluid dynamics (Schmid, 2010) and recently used to model temporal oscillations of electroencephalography (EEG) (Brunton et al., 2016a) and functional Magnetic Resonance Imaging (fMRI) data (Casorso et al., 2018) in the brain. DMD finds coherent spatio-temporal patterns in high-dimensional non-linear systems (details about DMD algorithms are included in the Method section). There are several unique advantages of DMD compared to other model fitting and multivariate approaches: 1) it is a data-driven method that does not require a fixed set of governing equations or prior assumptions of the underlying dynamics; 2) it combines the advantages from two frequently used analysis methods: PCA for the reduction of high-dimensional data and spectral time-series analysis for identifying the oscillation frequency of time-varying signals; 3) it can model non-linear systems effectively, unlike PCA which assumes that the relationships between variables is linear; 4) it can isolate/decompose the overall temporal course into specific dynamics (Proctor and Eckhoff, 2015; Taira et al., 2017). Instead of applying DMD to sequential time-series data in the frequency domain as is the case for EEG and fMRI data, we propose to extend DMD to model temporal changes of spatial patterns of tracer binding values as disease progresses.

To test the applicability and robustness of DMD to extract spatio-temporal patterns of tracer binding values, we first applied DMD to study dopaminergic denervation in Parkinson's disease (PD) using [^{11}C](±)dihydrotetrabenazine (DTBZ—a vesicular monoamine transporter type 2 (VMAT2) marker) PET. The motor deficit of PD is traditionally associated with dysfunction of the nigrostriatal pathway, characterized by progressive loss of dopaminergic neurons in the substantia nigra and loss of their projection fibres to the striatum (Stoessl, 2012). Neurodegeneration of the dopaminergic system tends to follow a fairly well defined spatio-temporal pattern in which the dorsal posterior putamen contralateral to the more affected body side is affected first, followed by degeneration in the ventral and anterior putamen and the caudate, as shown in Fig. 1 (Stoessl, 2012). PET studies have shown an exponential decline of dopaminergic terminals as disease progresses, where the rate of loss is highest in early disease (Lee et al., 2004; Nandhagopal et al., 2009). This is in broad agreement with post-mortem studies of nigral cell counts (Kordower et al., 2013) and striatal tyrosine hydroxylase immunoreactivity (Alerte et al., 2008). Using longitudinal and cross-sectional PET data, our group previously showed that while initial *levels* of dopaminergic loss were different, the *rates* of dopaminergic loss were similar in different striatal regions. It was therefore suggested that mechanisms responsible for disease progression (rate of loss) and disease initiation (initial severity of loss) may be different (Lee et al., 2004; Nandhagopal et al., 2009). It is thus expected that these distinct mechanisms may be reflected by distinctive spatio-temporal patterns in the striatum, which could be captured by DMD.

2. Materials and methods

2.1. Study participants

This study included 41 PD subjects with disease duration ranging from 0 to 16 years. Disease duration was estimated as time from onset of motor symptoms as reported by the subjects. PD subjects were clinically evaluated using the Movement Disorder Society Unified Parkinson's Disease Rating Scale Part III (MDS-UPDRS Part III) and Hoehn and Yahr scale to assess motor dysfunction. All PD subjects were cognitively normal as assessed by Montreal Cognitive Assessment (MoCA) (MoCA scores greater than 26). Detailed clinical characteristics are listed in Table 1. All assessments were performed off medication. The study was approved by the Clinical Research Ethics Board of the University of British Columbia and all subjects provided informed written consent.

2.2. Scanning protocols

All study subjects underwent DTBZ PET scans and a T1-weighted MRI scan of the brain. The PET scans were performed on a Siemens High Resolution Research Tomograph (HRRT, Knoxville, TN) with a spatial resolution of (2.5 mm)^3 (Jong et al., 2007). Subjects were positioned using external lasers aligning the gantry with the inferior orbital-external meatal line, and custom fitted thermoplastic masks were applied to minimize head movement. Prior to PET scans, subjects were withdrawn from all anti-parkinsonian medications for at least 12 h. 320 ± 34 MBq of (+)DTBZ were administered by intravenous injection over 60 s using an infusion pump (Harvard Instruments). Acquired data were binned into 16 time frames (frame durations: 4 × 60 s, 3 × 120 s, 8 × 300 s, 1 × 600 s; image dimension = 256 × 256 × 207; voxel size = (1.22 mm)^3) with a total duration of 60 min. Transmission scans required for attenuation correction were performed over ten minutes with a rotating ^{137}Cs source. PET images were reconstructed using the 3D sinogram Poisson Ordered Subset Expectation Maximization (OP-OSEM) algorithm (Comtat et al., 2004) with 16 subsets and six iterations, with corrections for decay, dead-time, normalization, attenuation, scattered and random coincidences. After reconstruction, images were smoothed with a 2.0-mm full-width at half maximum (FWHM) Gaussian filter to reduce noise. The frames were spatially realigned with rigid-body transformation to minimize the impact of motion during scans. The structural MRI scans were performed on a Philips Achieva 3.0T MRI scanner (Phillips Healthcare, Best, NL) using the T1 turbo field echo (TFE) sequence (TR/TE = 7.7/3.6 ms; TFE shots = 218; flip angle = 8°; image dimension: 256 × 256 × 170; voxel size (1 mm)^3).

2.3. Image processing

Parametric DTBZ binding images were generated with a previously published analysis pipeline (Klyuzhin et al., 2018). To optimize the co-registration and warping quality, we used a two-step registration pipeline. In the first step, the MRI images were first resampled to match the PET voxel size. DTBZ PET images averaged over 30–60 min post-injection were then rigidly co-registered to the corresponding subject's MR images using SPM12 software (Wellcome Department of Cognitive Neurology, University College London, UK). The quality of the co-registration was visually inspected. The MRI images were segmented to create masks for the striatal and the reference region (occipital cortex) using Freesurfer (Fischl et al., 2002). Parametric activity ratio (AR) images were generated by dividing the voxel values in the respective activity images by the mean activity in the reference region. Co-registered MRI and AR images were separated into more and less affected brain sides, contralateral to the more and less clinically affected body sides (based on MDS-UPDRS III total scores). In the second step, for each side separately, MRI-defined segmentation (Freesurfer) of the

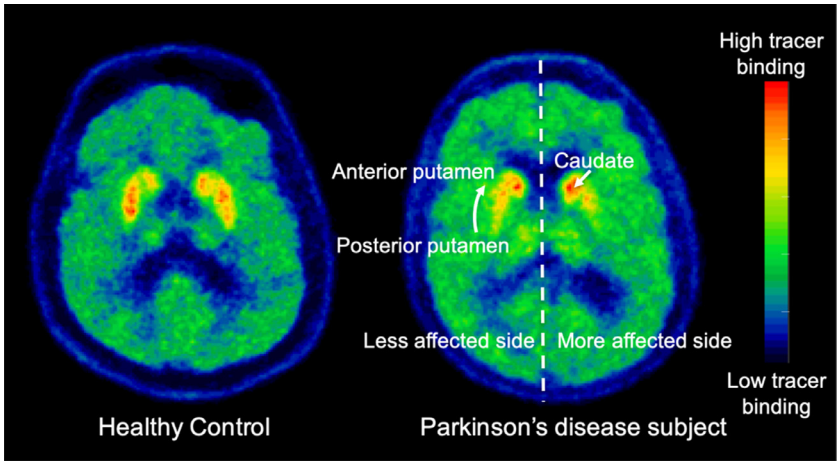

Fig. 1. [^{11}C](±)dihydrotetrabenazine (DTBZ) PET image for a healthy control (left) and a Parkinson's disease (PD) subject (right). PD subject showed characteristic asymmetric tracer uptake in the less and more affected sides and a spatio-temporal pattern of dopaminergic loss with the posterior putamen affected before the anterior putamen and caudate. PET = Positron Emission Tomography.

Table 1
Clinical characteristics of all subjects. All numbers are reported as mean ± standard deviation.

	Number	Sex	Age (years)	Disease duration (years)	H&Y	Total MDS-UPDRS III	MoCA
PD	41	25M/16F	61.8 ± 8.7	5.32 ± 4.31	1.9 ± 0.5	19.3 ± 10.5	28.0 ± 1.3

Disease duration estimated as the 1time from onset of motor symptoms as reported by the patients. PD = Parkinson's disease subjects; MDS-UPDRS = Movement Disorder Society Unified Parkinson's Disease Rating Scale; MoCA = Montreal Cognitive Assessment; H&*Y* = Hoehn and Yahr scale.

putamen and caudate were combined to generate a single labeled volume mask that was warped to a common striatal template using 3D diffeomorphic mapping (Fischl et al., 2002). The resulting transformation matrix was saved and applied to the respective AR images.

3. Introducing DMD

We first briefly summarize the DMD algorithm in Section 3.1 (Brunton et al., 2016b; Tu et al., 2013) . Application of DMD in the context of neuroimaging to model disease progression is illustrated in Section 3.2 with a brief explanation of meaningful outcome measures. Tests for robustness and reproducibility of DMD results are shown in Section 3.3. Comparison between the results obtained with DMD, univariate analysis and PCA can be found in the Section 3.4 and Section 3.5.

3.1. DMD algorithm

Consider measurements taken from n features at times kΔt, where k is the index of the temporal snapshots and Δt is the time difference between each snapshot (temporal resolution/sampling rate). Measurements from each temporal snapshot are arranged in a column vector x_k (size n by 1, $k = 1 \ldots t$, t is the index of last time point). Construct two matrices X_t and X_{t-1} (both are size n by $t-1$) as time-shifted versions of each other (shifted by Δt):

$$X_{t-1} = [x_1 \ \ldots \ x_{t-1}]$$

$$X_t = [x_2 \ \ldots \ x_t]$$

The progression from X_{t-1} to X_t (temporally progressed by Δt) is governed by an unknown linear operator A:

$$X_t = AX_{t-1} + \epsilon_t$$

where ϵ_t is the model residual or noise.

DMD models a high-dimensional linear regression of the non-linear dynamics relating X_t and X_{t-1} by the eigendecomposition of the operator A. To estimate A (size n by n), singular value decomposition is first applied to X_{t-1} so that:

$$X_t \approx AX_{t-1} = AU\Sigma V^*$$

where U (size n by r, where r is the number of reduced dimension), Σ (size r by r) and V (size t-1 by r) are the left-singular vectors, singular values and right-singular vectors of X_{t-1}.

Then

$$A \approx X_t X_{t-1}^{\dagger} = X_t V \Sigma^{-1} U^*$$

where $X_{t-1}^{\dagger}$ is the pseudoinverse of X_{t-1}.

However when n is large, direct eigenvalue analysis of A can be computationally expensive. A more efficient model is to project A into the reduced dimensional space with the operator U. Now we define the reduced order model $\tilde{A}$:

$$\tilde{A} = U^* A U = U^* X_t V \Sigma^{-1}$$

And the eigendecomposition of $\tilde{A}$ (size r by r) is:

$$\tilde{A} W = \Lambda W$$

where W (size r by r) is the eigenvectors and the diagonal of Λ contains *DMD eigenvalues* λ. Note that the eigenvalues for A and $\tilde{A}$ are identical, and their eigenvectors are associated by a linear transformation.

DMD modes (eigenvectors of A, size n by r) are defined as:

$$\Phi = X_t V \Sigma^{-1} W$$

The temporal dynamic curve is defined as:

$$T(t) = e^{\Omega t} z$$

$$\Omega = \log \Lambda / \Delta t$$

$$x_1 = \Phi \ z$$

where z (*DMD amplitude*, unitless) is used to scale the DMD mode (Φ) to match the input data at the first time point x_1. Since Λ can be real or complex valued, the temporal dynamic curve shows an exponential behaviour when Λ is real and shows an oscillatory behaviour when Λ is complex.

We can then approximate X with a dynamic model:

$$\hat{X}(t) = \Phi \ e^{\Omega t} z$$

The main message is that DMD decomposes the data into coupled spatio-temporal patterns: spatial modes (Φ) and their corresponding temporal dynamics (T(t)).

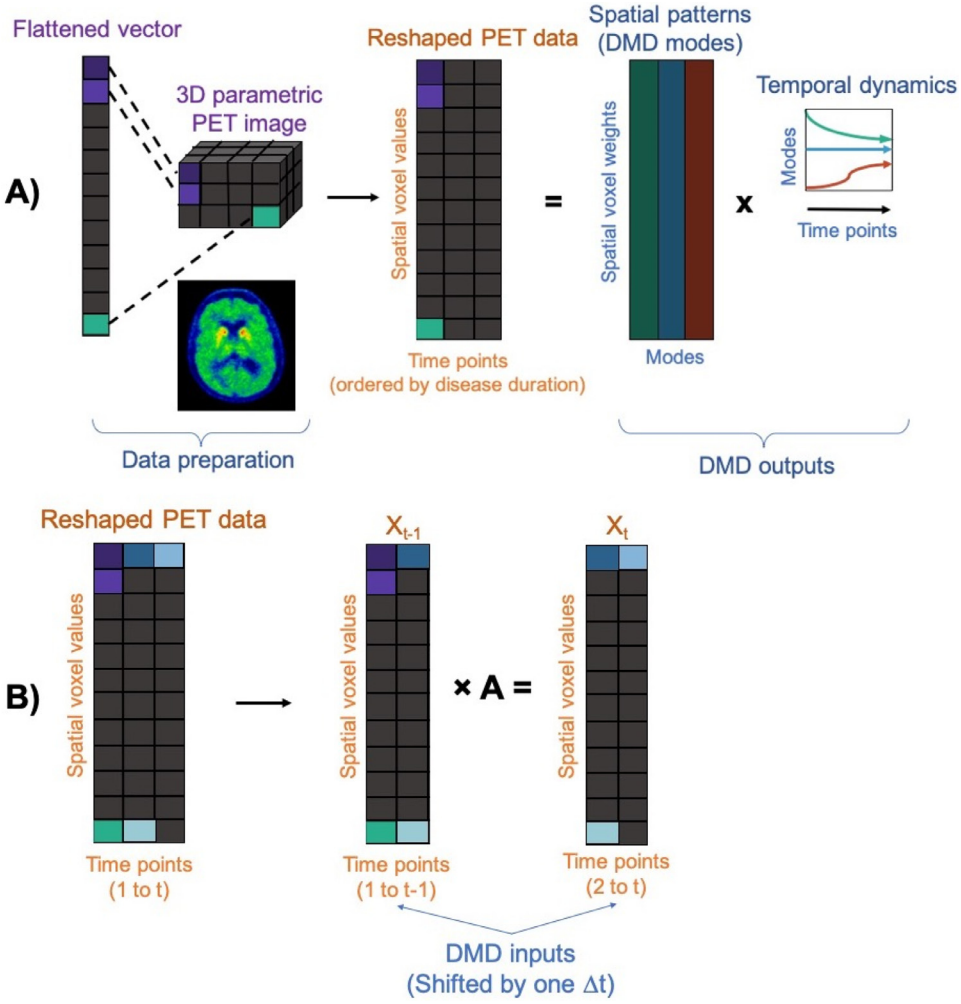

Fig. 2. Schematic diagram for dynamic mode decomposition (DMD) analysis pipeline. (A) In the data preparation step, the 3D parametric PET tracer binding image of each subject is stretched into a flattened column vector. Each column vector is then concatenated horizontally according to the disease durations of all subjects. DMD then decomposes the reshaped PET data into DMD modes (spatial patterns), each associated with an unique temporal dynamic curves. (B) The reshaped PET data are used to construct X_{t-1} and X_t matrices as time shifted version of each other, which are then used as input to DMD. PET = Positron Emission Tomography.

3.2. DMD applied to DTBZ PET data to track disease progression

Unlike fMRI and EEG data, where each temporal snapshot is a single scan from the dynamic time-series, here we want to model disease progression; we used cross-sectional data of subjects with different disease durations to represent temporal snapshots of the disease course (Fig. 2A). We first stretched each 3D parametric AR image into a long vector x_k (size n by 1, n is the total number of voxels in the AR image, k = 1…t) then temporally concatenated all k vectors according to their disease durations (in years) such that (Fig. 2B):

$$X_{t-1} = [x_1 \ \ldots \ x_{t-1}]$$

$$X_t = [x_2 \ \ldots \ x_t]$$

where x_1 represents the AR image vector for a subject with a disease duration of one year.

For time points with several snapshots (i.e. AR images of subjects with the same disease duration), we used the averaged AR images as a single snapshot. Each DMD mode represents a spatial pattern of dopaminergic denervation associated with a particular exponential growth/decay curve or an oscillatory temporal curve around zero (as a result of complex Λ values). Only DMD modes with real Λ values were considered, and DMD modes with oscillatory behaviour were considered as noise. It is also important to note that DMD *spatial* modes are not orthogonal/independent, while the orthogonality of DMD remains in the temporal domain, i.e. the temporal courses are orthogonal (loosely independent) to one another.

We applied DMD separately to the putamen and caudate as there might be different spatio-temporal patterns in the two striatal regions and we wanted to examine the effect of disease in each striatal substructure separately. We also applied DMD first separately to the less and more affected sides to investigate progression within a lateralized structure, then to both sides together to examine if the known denervation asymmetry associated with PD (especially in the early stages) would influence the spatial patterns and their temporal courses.

The analysis pipeline was written in Matlab and is available upon direct request to the corresponding author, however PET data used in this study are not made available publicly for reasons of patient confidentiality.

3.3. Robustness and reproducibility of DMD

For imaging studies, where the number of subjects may be relatively limited, the patient population may not fully sample the disease progression spectrum, resulting in missing time points on the disease time course. In our case, we did not have any subject with nine and 14 years of disease duration. We performed leave-one-out cross validation on the temporal snapshots to examine the effect of missing time points on the DMD outputs. In this study, the sampling rate of one was used which

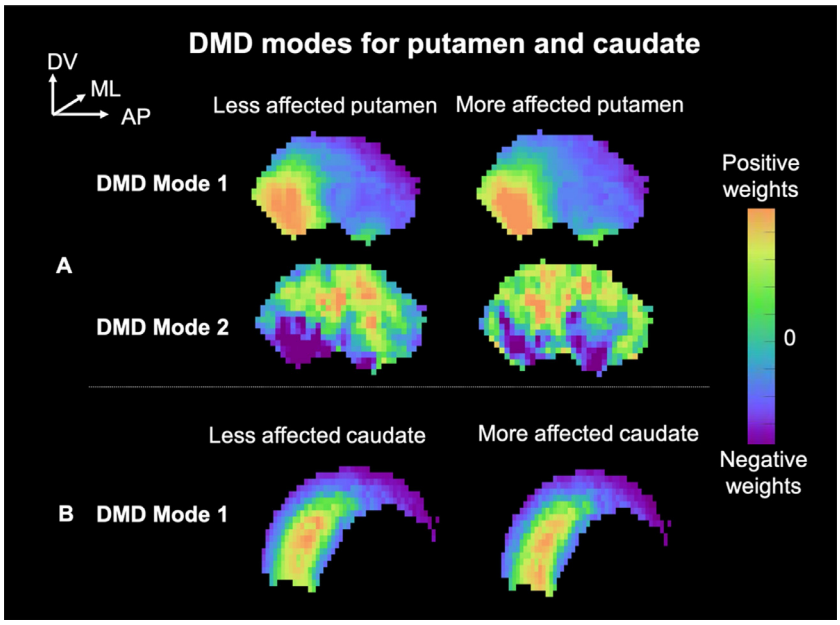

Fig. 3. DMD modes (spatial patterns) in the less and more affected putamen (A) and caudate (B). DMD was applied to the less and more affected sides separately. In the putamen, DMD mode 1 showed an anterior-posterior gradient and DMD mode 2 showed a dorsal-ventral gradient in both the less and more affected sides. DMD mode 1 in the caudate showed a head-tail gradient in both the less and more affected sides. Spatial patterns are displayed as maximum intensity projection onto the entire region of interest. DMD = dynamic mode decomposition. LM = lateral-medial. AP = anterior-posterior. DV = dorsal-ventral.

corresponds to one year disease duration step.

3.4. Univariate analysis

In addition to the multivariate analysis, we also fitted a pre-defined exponential function to the average DTBZ AR values in the less and more affected putamen and in the less and more affected caudate to compare the extracted DMD temporal curves with the models fitted to the average AR values.

The following exponential equation was fitted to the putamen:

$$Y(t) = a\ e^{-b*t} + c\ e^{-d*t}$$

While the exponential equation fitted to the caudate was of the form:

$$Y(t) = a\ e^{-b*t}$$

Where a, b, c, and d are the fitting parameters, t is disease duration (in years) and Y is the average AR values.

We used a pre-defined function with two exponential terms for the putamen and one exponential term for the caudate to match the number of spatio-temporal patterns extracted by DMD.

We also performed correlation analyses between the temporal expressions of DMD mode 1, DMD mode 2 and the sum of DMD mode 1 and mode 2 and the averaged DTBZ AR values in the less and more affected putamen and in the less and more affected caudate.

3.5. Comparison between DMD and PCA

DMD and PCA are conceptually similar in the sense that both involve decomposition of the input data. However, DMD models coupled temporal-spatial patterns while PCA only models variance in the data without accounting for any temporal information. In other words, if the input signal is composed of two sources with different temporal courses, PCA may fail to un-mix the two sources. Mathematically, the first step of the DMD algorithm is the same as PCA, while the variable A captures the temporal dynamic of the PCA mode (U) from one time point to the next:

$$U_t = AU_{t-1}$$

To illustrate the impact of the differences between the two approaches on the outcomes, we applied both DMD and PCA to DTBZ AR values in the less affected putamen and compared the spatial patterns of DMD and PCA and their associated subject/temporal scores as a function of disease duration.

4. Results

DMD decomposed DTBZ PET data into two coupled sets of distinctive spatio-temporal patterns in the putamen and a single spatio-temporal pattern in the caudate. The temporal curves were highly robust as shown by the small variations obtained in the leave-one-out cross validation. We kept the first two pairs of coupled DMD modes and their temporal courses that accounted for 98% of total variance in the data for the putamen and the first pair of coupled DMD modes and their temporal courses that accounted for at least 96% of total variance for the caudate for further analysis. Temporal curves for later DMD modes showed mostly oscillatory behaviour around zero, so were considered as non-meaningful. An example of non-meaningful DMD mode with oscillatory behaviour can be found in the Supplementary Materials (Fig. S1, Section 1). Detailed fitting parameters for univariate exponential models fitted to the average DTBZ AR values in the putamen and caudate, and more detailed comparison between DMD and traditional analyses can also be found in the Supplementary Materials (Section 2). There were significant correlations between the averaged DTBZ AR values in the more and less affected putamen and caudate and expression of DMD mode 1, mode 2 and the sum of the two modes in the putamen and caudate ($P < 0.01$). The correlations between the averaged DTBZ AR and the expression of the sum of DMD mode 1 and 2 was the strongest which is expected since the temporal expression of the sum of the two DMD modes reflect the overall progression change in DTBZ binding. More detailed results for the correlation analysis between temporal expression of DMD modes and the averaged DTBZ AR values can be found in the Supplementary Materials (Section 4).

4.1. Putamen

In both the less and more affected putamen, the first DMD modes showed characteristic anterior-posterior gradients that were almost identical between the two sides (Fig. 3A). These anterior-posterior patterns were associated with temporal curves with almost identical decay constants for both the less and more affected putamen (Fig. 4A). The DMD amplitude (intercept of the temporal curves), however, was much higher in the less affected putamen compared to the more affected putamen.

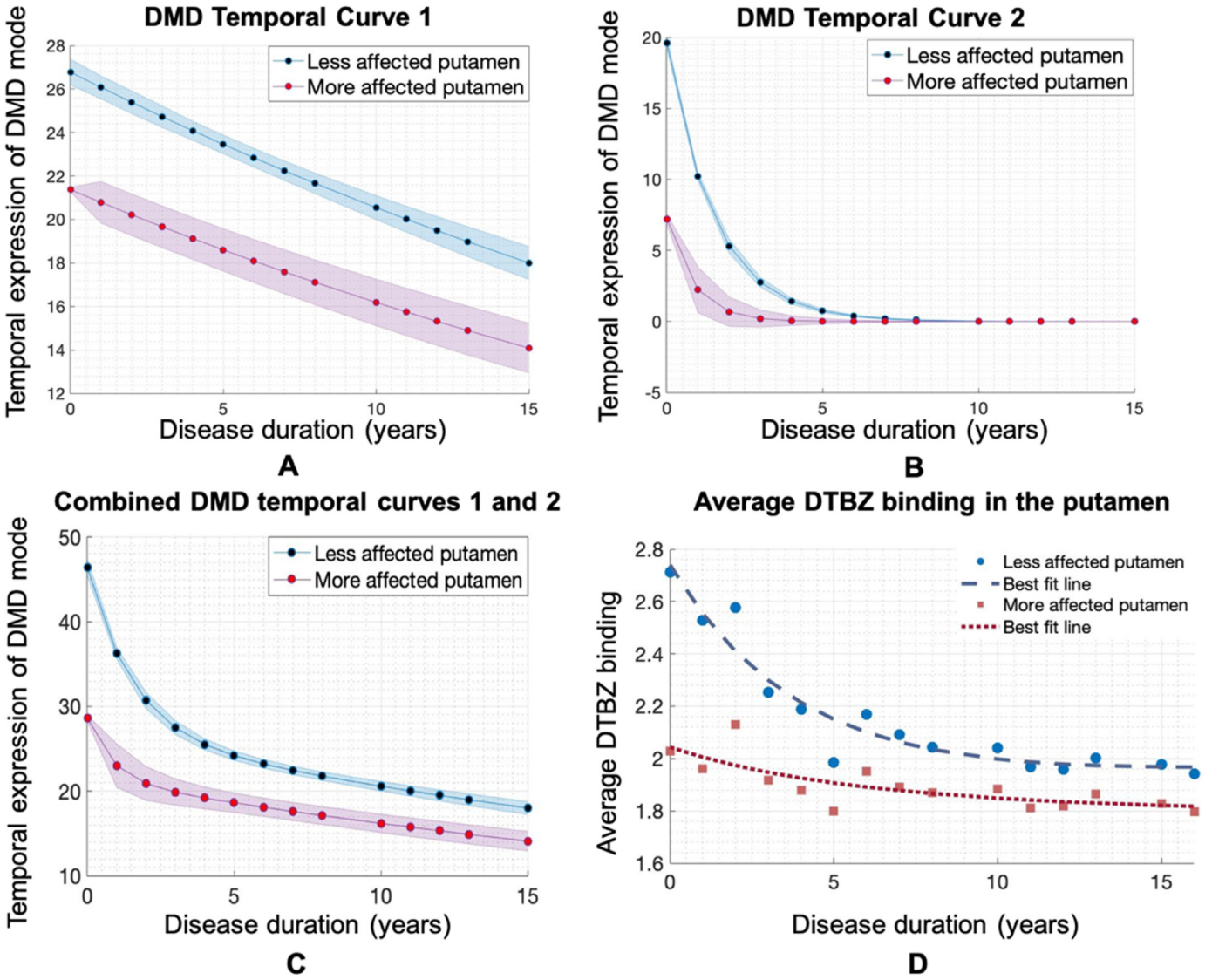

Fig. 4. (A) The first DMD temporal curve in the less and more affected putamen, associated with the anterior-posterior gradient. (B) The second DMD temporal curve in the less and more affected putamen, associated with the dorsal-ventral gradient. (C) Combined DMD temporal curves for the first and second DMD modes in the less and more affected putamen. (D) Averaged DTBZ activity ratios in the less and more affected putamen versus disease duration and the best exponential fit curve. Error bars were generated from leave-one-out cross validation. DMD = dynamic mode decomposition. DTBZ = dihydrotetrabenazine.

Table 2
DMD output parameters. All numbers are reported as mean ± standard deviation.

		Less affected Putamen	More affected Putamen	Less affected Caudate	More affected Caudate
Mode 1	DMD amplitude (z)	26.77 ± 0.69	21.38 ± 0.96	36.64 ± 0.17	33.14 ± 0.46
	Decay constant	−0.027 ± 0.004	−0.028 ± 0.005	−0.026 ± 0.002	−0.026 ± 0.004
Mode 2	DMD amplitude (z)	19.61 ± 0.42	7.22 ± 2.01	N/A	N/A
	Decay constant	−0.65 ± 0.05	−1.18 ± 0.18	N/A	N/A
Total variance explained (%)		97.7	97.7	96.2	97.0

DMD amplitudes (unitless) and decay constants determine the intercept and shape of the exponential temporal curves in each striatal region. Temporal curves with more negative decay constants drop more quickly with increasing disease duration compared to the temporal curves with decay constants closer to zero. The total percentage variance explained were calculated with the first two modes for putamen and with the first mode for caudate. Standard deviation of the DMD parameters were calculated from leave-one-out cross-validation. DMD = dynamic mode decomposition.

The second DMD mode showed a dorsal-ventral gradient in the less affected putamen (Fig. 3A) associated with a temporal curve that decreased sharply in the early stage of the disease (<5 years) (Fig. 4B). For the more affected putamen, the second temporal curve neared zero after approximately one year of disease duration (Fig. 4B). Detailed DMD output parameters are listed in Table 2.

Combining the temporal curves for the first two DMD modes (Fig. 4C), we observed that the initial progression rates and intercepts in the less and more affected putamen were quite different; the difference was mainly dominated by the second DMD mode (dorsal-ventral gradient). The progression rates then became similar in the less and more affected putamen as the first DMD mode (anterior-posterior

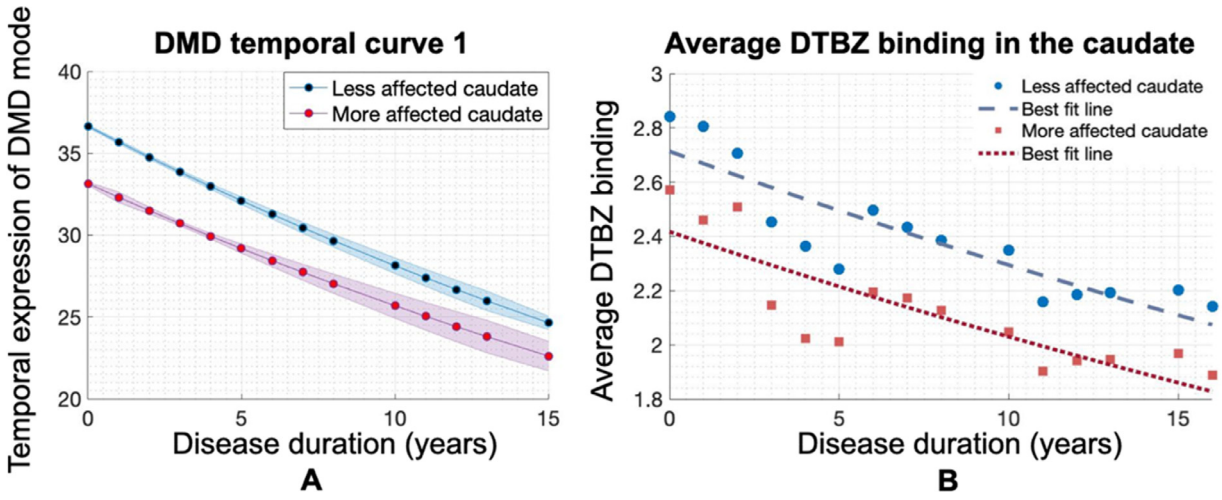

Fig. 5. (A) The first DMD temporal curve in the less and more affected caudate, is associated with the head-tail gradient. (B) Averaged DTBZ activity ratios in the less and more affected caudate versus disease duration and the best exponential fit curve. Error bars were generated from leave-one-out cross validation. DMD = dynamic mode decomposition. DTBZ = dihydrotetrabenazine.

gradient) started to dominate. The combined temporal curve also highly resembled the exponential function fitted to the averaged AR values in the less and more affected putamen (Fig. 4D).

4.2. Caudate

The first DMD modes showed a head-tail gradient in both the less and more affected caudate (Fig. 3B). This gradient was associated with temporal curves with almost identical decay constants in both the less and more affected caudate (Fig. 5A). The intercept for the temporal curves was higher for the less affected caudate than that for the more affected caudate, however, the differences in gradient expression became smaller as the two curves tended to converge in later disease stage. Again, this DMD temporal curve highly resembled the exponential function fitted to the averaged AR values in the less and more affected caudate (Fig. 5B).

We also applied DMD to both the less and more affected sides together in the caudate and putamen; spatial patterns and temporal curves were very comparable with those obtained by applying DMD to the less and more affected sides separately (Supplementary Materials, Section 3).

4.3. Comparison between DMD and PCA

As shown in Fig. 6, the first spatial patterns (DMD mode 1 and PCA pattern 1) obtained from DMD and PCA showed very similar anterior-posterior gradient in the less affected putamen; the relationship between the subject scores related to the PCA-defined spatial pattern and disease duration was however much less robust compared to the DMD temporal curve. The second spatial patterns showed slight dorsal-ventral gradient in the putamen for both DMD and PCA and very similar temporal expression of the patterns as a function of disease duration. The differences in the spatial patterns and scores between DMD and PCA were due to the additional temporal information embedded in the DMD algorithm. The similar distributions of DMD and PCA scores of pattern 2 suggest the second temporal component extracted by DMD also accounts for approximately the second largest variance (approximately 3.6% of variance accounted for by the second PCA pattern) in the data in this particular case.

5. Discussion

In this work, we showed the first application of DMD to visualize and quantify disease-induced progressive changes in neurotransmitter activities. We first described the implementation of DMD to extract spatio-temporal patterns related to disease progression using neuroimaging data and then tested the method on a well-established DTBZ PET dataset to model dopaminergic denervation in PD. The method was found to be robust with respect to typical uncertainties in the estimation of disease duration and is expected to be easily applicable to a wide range of imaging data.

This work presents both methodological and clinically relevant advances. In terms of methodological novelties, we presented the first multivariate approach that simultaneously models spatial and temporal patterns related to neurodegeneration using PET data. We compared the DMD temporal curves with a static multivariate approach (PCA) that only models spatial information in the data. We demonstrated that even though PCA and DMD showed similarities in the spatial patterns and temporal expression of the patterns as a function of disease duration, DMD was intrinsically able to more accurately extract spatial patterns with different progressive behaviours and thus provided a more powerful alternative dimension reduction method for modelingprogressive changes.

An important methodological advantage of the DMD approach is that the spatio-temporal patterns are derived in a purely data-driven and equation-free fashion at a voxel-level, which is especially important when the underlying disease mechanisms are unknown. When modeling temporal changes with traditional approaches, the choice of the final model is usually based on estimating model residuals or other objective methods such as the Akaike information criterion (Supplementary Materials, Section 2). DMD, on the other hand, automatically decomposes the data into an optimal number of exponential functions with minimal need for parameter tuning.

Another unique and important advantage of the DMD approach is its ability to decompose temporal changes of tracer binding into orthogonal (loosely implying independent) temporal trajectories; while the traditional approach (i.e. pre-defined model fitted to the averaged AR values in individual striatal regions) can only model the overall temporal changes by minimizing the least square error between the data and best fit curve. The spatial patterns associated with each independent temporal trajectory represent regions that change similarly as a function of disease duration: the method is thus able to identify regions that are differentially sensitive to potentially different disease mechanisms.

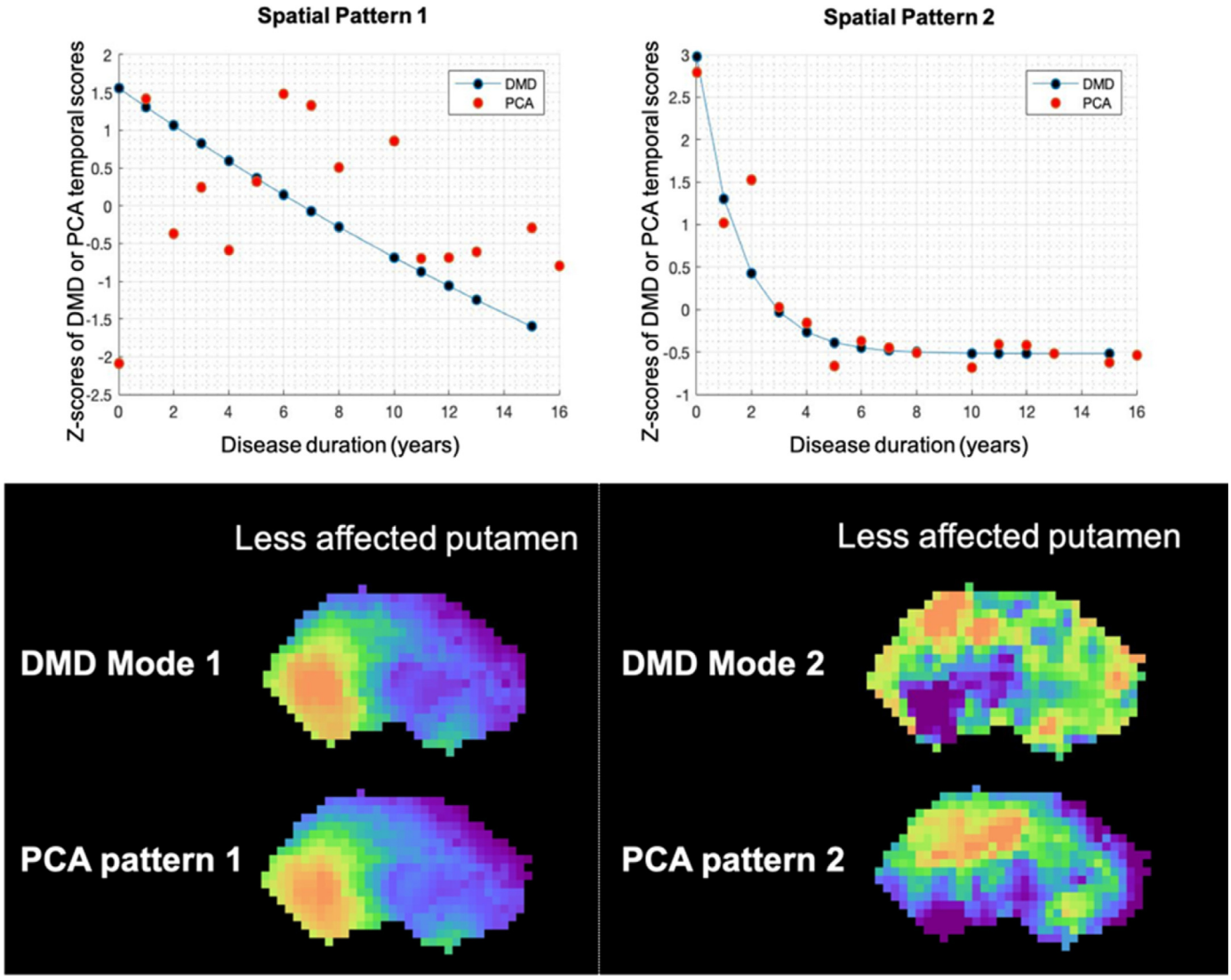

Fig. 6. Comparison between DMD temporal expression of mode 1 (left) and mode 2 (right) and PCA scores of PCA pattern 1 (left) and PCA pattern 2 (right) in the less affected putamen. Both DMD temporal expressions and PCA scores are Z-transformed. Spatial patterns are displayed as maximum intensity projection onto the entire region of interest. DMD = dynamic mode decomposition. PCA = principal component analysis.

5.1. DMD spatio-temporal patterns in the putamen and caudate

In this work, we were able to decompose the overall disease progression curve in the putamen into two independent temporal curves associated with distinct spatial patterns of dopaminergic denervation. The combined temporal expression of the anterior-posterior and dorsal-ventral gradients (Fig. 4C) showed striking resemblance to the disease progression curves previously presented using univariate measures in the putamen regions obtained with a different patient population on a different scanner (Nandhagopal et al., 2009) and the univariate exponential fit curves obtained with averaged DTBZ AR values in the putamen (Fig. 4D).

While the initial expression of the anterior-posterior gradient was higher in the less affected putamen, the expression of this gradient decreased gradually at similar rates in the less and more affected putamen and still existed in later disease stage (~ 15 years of disease duration) (Fig. 4A). This indicates that the anterior-posterior gradient is likely well maintained bilaterally over the disease course (Müller et al., 2000; Nandhagopal et al., 2009); the fact that the rate of decrease is the same on both sides provides further support to the interpretation that this pattern is related to mechanisms responsible for disease progression.

The dorsal-ventral gradient in the putamen, however, existed only in very early disease, mainly in the less affected side. Previous studies showed that the rate of dopaminergic neuron loss is highest in early disease and the level of asymmetry between the less and more affected sides is more prominent at this stage (Müller et al., 2000; Nandhagopal et al., 2009). According to our analysis, this rapid change of dopaminergic function in early disease may be mainly due to the changes along the dorsal-ventral gradient. It is interesting to note that the curves related to the less affected side seem to be shifted in time by approximately 5–8 years compared to the more affected side (by visual inspection), likely reflecting the asymmetric nature of disease onset followed by an asymmetric onset of clinical symptoms.

The expression of the head-tail gradient in the caudate decreased gradually with disease. The initial expression (intercept), however, was higher for the less affected caudate than the more affected caudate. This implies that even though there is an initial difference in the expression of this gradient in the less and more affected caudate at disease onset, there is no asymmetric progressive changes in the caudate along this gradient. However, the caudate (especially the tail) is particularly prone to partial volume effect, which may suggest that the head-tail gradient could be a result of 'spill-out' effect from the edge of the caudate to its surroundings; the reduction in temporal expression for

this DMD mode may therefore only reflects an overall magnitude change in tracer binding across the entire caudate rather than a true head-tail gradient in the caudate. To partially address this issue, we compared the decay constants from the DMD temporal curve and the exponential model fitted to the averaged AR values in the entire caudate as a function of time. The decay constants from the exponential fits were -0.018 and -0.017 for the more and less affected caudate respectively (Table S1), which were larger than the decay constants for the head-tail gradient extract by DMD, which implies the expression of the head-tail gradient decreases faster than the average tracer binding across the whole caudate. Even though this comparison does not fully address the potential confound due to partial volume effect, the differences in decay constants support that the decrease of the gradient is disease-related rather than an imaging artefact.

The decay constants for the anterior-posterior gradient in the putamen and the head-tail gradient in the caudate were very similar, providing further support to the interpretation that these two gradients of dopaminergic denervation may be due to non-specific mechanisms that affect all striatal sub-regions at a similar rate. The presence of a dorsal-ventral gradient in the putamen restricted to early disease may be related to either an independent disease-initiating mechanism or differential involvement of striatal sub-regions at different disease stages. Further studies are needed to relate the different spatio-temporal patterns with disease mechanisms.

While practically and conceptually consistent with earlier hypotheses on PD initiation/progression, the unique and more general contribution of this approach to the analysis of PET data is that the method appears to be able to separate independent temporal patterns of disease progression and identify the regional contributions to each of such patterns. It thus provides more direct evidence for the existence of different disease-related mechanisms and an assessment of their topological characteristics and relevance at different stages of disease, thus providing much more detailed information compared to traditional analysis methods.

5.2. Limitations

There are several limitations of this study. The first major limitation is the relatively small sample size used in this study. Second, DMD assumes there is a fixed temporal resolution in the input data; we took the sampling rate (Δt) to correspond to one year of disease duration in our data. Since the uncertainty in the determination of disease duration in PD ranges from 0.5 to 1 year, we randomly shifted disease durations of all subjects by $\pm$ 1 year; the DMD outputs for the randomly shifted data did not change appreciably. Third, cross-sectional data were used to model disease progression, for which individual subject variability could represent a potential confounding factor. However, obtaining longitudinal data on the same subject at short disease intervals is often not practical. While we acknowledge that longitudinal data may provide a more accurate description of disease progression, previous studies showed very similar disease progression curves obtained with cross-sectional data alone (Lee et al., 2004; Lee et al., 2000) and with a mixture of cross-sectional and longitudinal data (Nandhagopal et al., 2009; Nandhagopal, 2011). The subject variabilities are partially accounted for by taking the averaged images over subjects with the same disease duration. More importantly, DMD models the overall progression across all time points, where each time point is represented by a different subject, so it is less sensitive to heterogeneity in disease progression between subjects compared to univariate analyses. Fourth, parametric AR images were used instead of non-displaceable binding potential (BP_{ND}) images as a measure of dopaminergic denervation; this choice was made out of convenience as these data were readily available. We previously applied PCA to both parametric AR and BP_{ND} images in a subset of the same subject cohort involved in this study; the resulting spatial patterns were virtually identical (Klyuzhin et al., 2018). In principle, DMD can be applied to different types of parametric images, since it primarily works with covariance patterns rather than absolute voxel values. Fifth, even though striatal VMAT2 is predominantly expressed on dopaminergic nerve terminals, it is also expressed on other monoaminergic neurons. However, DMD may be less sensitive to confounds introduced by the lack of tracer selectivity compared to traditional analyses. In principle, DTBZ sourced from different nerve terminals (i.e. dopaminergic and non-dopaminergic) should follow different temporal progression curves, which could potentially be captured by DMD.

6. Conclusion

In this work, we introduced the DMD approach to PET data and demonstrated that this approach is able to capture spatio-temporal patterns of dopaminergic denervation in PD. This approach appears very well suited to model disease- or treatment-induced progressive changes in imaging data. This proposed method has several advantages over traditional methods in terms of biologically-relevant information that can be extracted from the data: first, it considers tracer distributions in all the selected regions at once, thus providing information not only on localized alterations, but also on spatial patterns of such alterations, emphasizing the network behaviour of the targets under investigation. Second, this approach incorporates both spatial and temporal information simultaneously in a data-driven and equation-free fashion. Thirdly, it allows the decomposition of overall disease-induced progression into orthogonal temporal curves, possibly relating to independent mechanisms. In this study, we were able to, for the first time, decompose the dopaminergic denervation in the striatum associated with PD into two spatio-temporal patterns: (i) the anterior-posterior gradient in the putamen and head-tail gradient in the caudate, which may be related to non-specific mechanisms responsible for disease progression and (ii) the dopaminergic denervation along the dorsal-ventral gradient in the putamen which may reflect independent mechanisms responsible for disease initiation in the very early stage of the disease. While the data considered in this study allowed us to validate this approach and provide some novel insights into PD progression, the method can be easily applied to data obtained with other tracers and related to other diseases.

Author contributions

VS and AJS designed the study. IK contributed to data preprocessing. JF and MM contributed to method development. JF and VS contributed to design and draft of the manuscript. AJS, MM and IK gave critical comments on the manuscript. All the authors read and gave final approval of the manuscript to be published.

Declaration of Competing Interest

The authors do not have any conflict of interest to report.

Acknowledgments

The authors thank the UBC PET scanning and the TRIUMF radiochemistry production staff. The volunteer subjects who generously donated their time to this research are also most gratefully acknowledged. The study was financially supported by the Natural Sciences and Engineering Research Council of Canada (NSERC) [grant number 240670-13], Brain Canada [grant number 64457], and Canadian Institutes of Health Research (CIHR) [grant number 125989]. AJS is supported by the Canada Research Chairs program. JF receives scholarship funding from the Isotopes for Science and Medicine program (NSERC-CREATE).

Supplementary materials

Supplementary material associated with this article can be found, in the online version, at doi:10.1016/j.nicl.2019.102150.

References

Alerte, T.N.M., Akinfolarin, A.A., Friedrich, E.E., Mader, S.A., Hong, C.-S., Perez, R.G., 2008. α-Synuclein aggregation alters tyrosine hydroxylase phosphorylation and immunoreactivity: lessons from viral transduction of knockout mice. Neurosci. Lett. 435, 24–29. https://doi.org/10.1016/J.NEULET.2008.02.014.

Badoud, S., Nicastro, N., Garibotto, V., Burkhard, P.R., Haller, S., 2016. Distinct spatiotemporal patterns for disease duration and stage in Parkinson's disease. Eur. J. Nucl. Med. Mol. Imaging 43, 509–516. https://doi.org/10.1007/s00259-015-3176-5.

Brunton, B.W., Johnson, L.A., Ojemann, J.G., Kutz, J.N., 2016a. Extracting spatial–temporal coherent patterns in large-scale neural recordings using dynamic mode decomposition. J. Neurosci. Methods 258, 1–15. https://doi.org/10.1016/J.JNEUMETH.2015.10.010.

Brunton, B.W., Johnson, L.A., Ojemann, J.G., Kutz, J.N., 2016b. Extracting spatial–temporal coherent patterns in large-scale neural recordings using dynamic mode decomposition. J. Neurosci. Methods 258, 1–15. https://doi.org/10.1016/j.jneumeth.2015.10.010.

Casorso, J., Kong, X., Chi, W., Van De Ville, D., Yeo, B.T.T., Liégeois, R., 2018. Dynamic mode decomposition of resting-state and task fMRI. 10.1101/431718.

Colloby, S.J., Williams, E.D., Burn, D.J., Lloyd, J.J., McKeith, I.G., O'Brien, J.T., 2005. Progression of dopaminergic degeneration in dementia with Lewy bodies and Parkinson's disease with and without dementia assessed using 123I-FP-CIT SPECT. Eur. J. Nucl. Med. Mol. Imaging 32, 1176–1185. https://doi.org/10.1007/s00259-005-1830-z.

Comtat, C., Bataille, F., Michel, C., Jones, J.P., Sibomana, M., Janeiro, L., Trebossen, R., 2004. OSEM-3D reconstruction strategies for the ECAT HRRT. In: Proceeding of the IEEE Symposium Conference Record Nuclear Science 2004, pp. 3492–3496. https://doi.org/10.1109/NSSMIC.2004.1466639.

Fischl, B., Salat, D.H., Busa, E., Albert, M., Dieterich, M., Haselgrove, C., van der Kouwe, A., Killiany, R., Kennedy, D., Klaveness, S., Montillo, A., Makris, N., Rosen, B., Dale, A.M., 2002. Whole brain segmentation: automated labeling of neuroanatomical structures in the human brain. Neuron 33, 341–355. https://doi.org/10.1016/s0896-6273(02)00569-x.

Jong, H.W.A.M.de, Velden, F.H.P.van, Kloet, R.W., Buijs, F.L., Boellaard, R., Lammertsma, A.A., 2007. Performance evaluation of the ECAT HRRT: an LSO-LYSO double layer high resolution, high sensitivity scanner. Phys. Med. Biol. 52, 1505–1526. https://doi.org/10.1088/0031-9155/52/5/019.

Klyuzhin, I.S., Fu, J.F., Hong, A., Sacheli, M., Shenkov, N., Matarazzo, M., Rahmim, A., Jon Stoessl, A., Sossi, V., 2018. Data-driven, voxel-based analysis of brain PET images: application of PCA and LASSO methods to visualize and quantify patterns of neurodegeneration. PLoS ONE 13. https://doi.org/10.1371/journal.pone.0206607.

Klyuzhin, I.S., Fu, J.F., Shenkov, N., Rahmim, A., Sossi, V., 2019. Use of generative disease models for analysis and selection of radiomic features in pet. IEEE Trans. Radiat. Plasma Med. Sci. 3, 178–191. https://doi.org/10.1109/TRPMS.2018.2844171.

Kordower, J.H., Olanow, C.W., Dodiya, H.B., Chu, Y., Beach, T.G., Adler, C.H., Halliday, G.M., Bartus, R.T., 2013. Disease duration and the integrity of the nigrostriatal system in Parkinson's disease. Brain 136, 2419–2431. https://doi.org/10.1093/brain/awt192.

Lee, C.S., Samii, A., Sossi, V., Ruth, T.J., Schulzer, M., Holden, J.E., Wudel, J., Pal, P.K., De La Fuente-Fernandez, R., Calne, D.B., Stoessl, A.J., 2000. In vivo positron emission tomographic evidence for compensatory changes in presynaptic dopaminergic nerve terminals in Parkinson's disease. Ann. Neurol. 47, 493–503 doi:10.1002/1531-8249(200004)47:4<493::AID-ANA13>3.0.CO;2-4.

Lee, C.S., Schulzer, M., De La Fuente-Fernandez, R., Mak, E., Kuramoto, L., Sossi, V., Ruth, T.J., Calne, D.B., Stoessl, A.J., 2004. Lack of regional selectivity during the progression of Parkinson disease: implications for pathogenesis. Arch. Neurol. 61, 1920–1925. https://doi.org/10.1001/archneur.61.12.1920.

Müller, J., Wenning, G.K., Jellinger, K., McKee, A., Poewe, W., Litvan, I., 2000. Progression of HOEHN and YAHR stages in parkinsonian disorders: a clinicopathologic study. Neurology 55, 888–891. https://doi.org/10.1212/WNL.55.6.888.

Nandhagopal, R., Kuramoto, L., Schulzer, M., Mak, E., Cragg, J., Lee, C.S., McKenzie, J., McCormick, S., Samii, A., Troiano, A., Ruth, T.J., Sossi, V., De La Fuente-Fernandez, R., Calne, D.B., Stoessl, A.J., 2009. Longitudinal progression of sporadic Parkinson's disease: a multi-tracer positron emission tomography study. Brain 132, 2970–2979. https://doi.org/10.1093/brain/awp209.

Nandhagopal, R., Kuramoto, L., Schulzer, M., Mak, E., Cragg, J., McKenzie, J., McCormick, S., Ruth, T.J., Sossi, V., De La Fuente-Fernandez, R., Stoessl, A.J., 2011. Longitudinal evolution of compensatory changes in striatal dopamine processing in Parkinson's disease. Brain 134, 3290–3298. https://doi.org/10.1093/brain/awr233.

Proctor, J.L., Eckhoff, P.A., 2015. Discovering dynamic patterns from infectious disease data using dynamic mode decomposition. Int. Health 7, 139–145. https://doi.org/10.1093/inthealth/ihv009.

Schmid, P., 2010. Dynamic mode decomposition of numerical and experimental data. J. Fluid Mech 656, 5–28 doi:10.1017/s0022112010001217i.

Stoessl, A.J., 2012. Neuroimaging in Parkinson's disease: from pathology to diagnosis. Parkinsonism Relat. Disord. 18 (Suppl 1), S55–S59. https://doi.org/10.1016/S1353-8020(11)70019-0.

Taira, K., Brunton, S.L., Dawson, S.T.M., Rowley, C.W., Colonius, T., McKeon, B.J., Schmidt, O.T., Gordeyev, S., Theofilis, V., Ukeiley, L.S., 2017. Modal analysis of fluid flows: an overview. AIAA J 55, 4013–4041. https://doi.org/10.2514/1.J056060.

Tu, J.H., Rowley, C.W., Luchtenburg, D.M., Brunton, S.L., Kutz, J.N., 2013. On dynamic mode decomposition: theory and applications. 10.3934/jcd.2014.1.391.